Thermal-Transport, Stability, and Irreversibility in Shrinking MHD Rotating-Disk Systems with Nonlocal Heat Flux and Arrhenius Reactivity

John Michael Owen[1]

[1] Emeritus Professor of Aerospace Engineering / Department of Mechanical Engineering, University of Bath
* Correspondence: J.M.Owen@bath.ac.uk

Abstract: In this study, we propose an engineering-scale similarity model of magnetohydrodynamics (MHD)-induced unsteady shrinking rotating disk flow subject to Cattaneo–Christov heat flux, Arrhenius chemical reaction, viscous dissipation, joule heating, and temperature-dependent viscosity. The model system constitutes an idealization of thermal machinery operated by mechanical rotation, where flow dynamics, heat transfer on the wall, and entropy generation all govern permissible performance limits and transport efficiency. In the formulation, the shrinking parameter λ plays the role of the continuation parameter, whereas the radial wall shear stress $F'(0)$ is selected as the indicator for the onset of bifurcation. The fold point is analyzed using singularity theory through the identification of singularities, one-dimensional kernels, and transversality conditions; the reduction of the problem through the Lyapunov–Schmidt procedure reveals the canonical square root dependence of the critical parameter around the saddle-node bifurcation point. Using adaptive collocation with continuation, numerical computations are performed to obtain steady-state solutions, wall shears and transfers, and the spectral value associated with the largest time-decay rate of the linearized problem. From the obtained results, a conservative continuation threshold λ_c^{scan} in agreement with the fold-point behavior is determined, demonstrating the strong influence of the Cattaneo–Christov heat flux model on the temperature and entropy generation distributions but a minor effect on the flow dynamics at the wall. Decomposition of the entropy generation into the thermal, viscous, and magnetic parts and determination of the Bejan number reveal how finite heat transport contributes to entropy generation in the boundary layer.

Keywords: rotating-disk flow; Cattaneo–Christov heat flux; magnetohydrodynamics; thermal relaxation; fold bifurcation; entropy generation; mechanical engineering transport systems

Citation: John Michael Owen. 2021. Thermal-Transport, Stability, and Irreversibility in Shrinking MHD Rotating-Disk Systems with Nonlocal Heat Flux and Arrhenius Reactivity. *TK Techforum Journal (ThyssenKrupp Techforum)* 2021(2): 1–17.

Received: January-23-2021
Accepted: July-20-2021
Published: Sptember-30-2021

1. Introduction

Rotating-disk flows hold an exceptional place in fluid mechanics and mechanical engineering owing to the rare instance of exact similarity reduction for Navier–Stokes equations within this family of three-dimensional viscous flows. From the pioneering work of von Kármán [1] to modern applications, the rotating disk has remained a classic theoretical problem and an archetypal case for analyzing technologically relevant transport phenomena characterized by swirl, crossflow, centrifugal pumping, and wall-driven secondary motion [2–4]. In turbomachinery, the disk serves as an essential component in rotors, stators, cavities, and heat exchangers in which controlled use of rotation enhances convective transport and boundary layer manipulation [5]. In micro-scale electronics, rotating-disk setups provide an environment for advanced coating and wafer processing in spin coaters and thermal processing equipment [6]. Owing to the interplay between its exact structural similarity reduction and its nonlinear dynamic complexity, the rotating disk has continued to offer unique opportunities for studying the influence of modified constitutive relations, external forcings, and wall kinematics on the existence, multiplicity, stability, and performance limits of rotating systems.

Although it already displays many important physical features, the classical steady von Kármán problem provides a template for understanding the essential mechanisms at play in subsequent developments. Rotation drives fluid centrifugally away in the radial direction, while the resulting radial ejection is balanced by the induction of an axial inflow that maintains continuity at the wall. Crossflow is thus a defining characteristic of the problem and an indispensable ingredient for the emergence of bifurcations, instabilities, and multiplicity [7,8]. Later research showed that this basic problem possesses a high degree of robustness: it can incorporate effects of suction, magnetic damping, roughness, variable properties, imposed ambient rotation, and transient forcing, but still maintain the essential interplay between momentum transport and wall-normal entrainment [9]. This combination of mathematical elegance and dynamic subtlety has made the rotating disk an enduring reference setup for studies incorporating new constitutive transport laws.

Among the most recent developments in the rotating disk literature are the observations that wall kinematics may be contracting or shrinking, as well as that shrinkage can trigger solution multiplicity and saddle-node turning behavior in certain regimes. The effect of stretching wall motion is generally constructive: it regularizes near-wall behavior by pulling fluid along the wall in a direction that agrees with the dominant centrifugal transport mechanism. On the other hand, shrinking motion opposes the outward transport caused by the disk rotation and generates potential for strong wall reversal, overshoot, and competitive interactions between the convective mechanisms. As a result, the induced boundary-value problem is more difficult than a straightforward parameter perturbation of the von Kármán state. Recently several groups have studied dual solutions in the presence of various auxiliary transport phenomena, particularly in connection with rotating disks with variable viscosity or suction [10]. At the same time, it is known that in a shrinking flow the global nature, transient growth, and branch sensitivity of the solution structure must be understood from the operator perspective, rather than inferred from computed solution profiles [11–14]. The existing literature focuses on the presence of computed branches, while paying relatively little attention to the operator-based explanation for why these branches occur, how close the numerics approach the actual saddle-node bifurcation, and whether the branches are locally stable in the neighborhood of the exact turning point.

In another line of research, the increasing need for rapid heating and cooling, combined with advances in material science, have motivated the investigation of non-Fourier heat transport for thermal processing applications. The classical Maxwell–Cattaneo equation introduces a thermal relaxation time to overcome the unrealistic infinite propagation speed implied by Fourier's constitutive model [15]. Christov's improved reformulation incorporates a frame-indifferent convective derivative in place of the ordinary time derivative, embedding finite-speed heat transport in a constitutive law consistent with continuum kinematics [16]. In the literature, the Cattaneo–Christov relaxation term has been used to study heat transport in various physical contexts including thermal convection [17], viscous flow [18], and boundary layers [19,20]. For the present analysis, what is important is that the Christov amendment to Fourier's heat diffusion equation introduces differential couplings between thermal relaxation and diffusion that can affect the geometry and curvature of the thermal boundary layer.

While the introduction of thermal relaxation is conceptually significant, it is often treated as a profile modifier in many modern works on applied heat transfer rather than an active mechanism for changing the solution structure and geometry of coupled transport phenomena. This phenomenon is especially prominent in high-parameter studies involving highly parameterized rotating-disk or stretching-sheet flow setups to which additional elements such as viscous dissipation, magnetic forcing, slip, radiative heat transport, nanofluids, entropy generation, or activation energy have been added. Under such conditions, the discussion of the relaxation mechanism usually focuses on the resulting modification to the thermal profiles and Nusselt numbers, while its indirect influence on momentum due to temperature-dependent viscosity is implicitly assumed. Entropy generation can even be calculated, but often only as a secondary outcome rather than a

diagnostic tool that reveals the redistribution of irreversibility induced by the relaxation mechanism [21]. This situation is more pronounced in shrinking boundary layer flow, in which the local dynamics are already complicated by wall-induced reversing motion and near-fold behavior.

This study seeks to address the above-mentioned gap in the literature. The focus is on the following question: how does thermal relaxation manifest in the coupled momentum-temperature system when energy and momentum are connected by means of thermoviscous feedback? This is a mathematically meaningful question since the relaxation term will not appear in the momentum equation without the constitutive dependency between energy and momentum transport. By making viscosity temperature-dependent, the analyst opens the door for the relaxation mechanism to affect the radial and azimuthal momentum equations through indirect couplings and influence the dynamics of the momentum problem. The significance of this indirect coupling justifies detailed examination, independent of the temperature profiles.

As another motivation for the present analysis, it is noted that rotating-disk flows are often used as an archetype for studying stability problems since their three-dimensional boundary layer admits crossflow-type instabilities and branch-dependent evolution [22]. The presence of solution multiplicity and the associated saddle-node bifurcations in the shrinking disk flows have made it customary to identify the two computed branches as "stable" and "unstable" based on their respective spectra. While this distinction is useful, it sometimes leads to an oversimplified view of what is actually computed numerically. Namely, the computed states are labeled "stable" or "unstable" on the basis of their linear spectra, but do not necessarily reconstruct the overall solution structure in the vicinity of the saddle node. To avoid overstating what the numerics actually achieve, it is desirable to report the spectral data and classify the eigenvalue problem in a way consistent with the numerics.

Finally, the inclusion of relaxation and thermoviscous feedback offers another opportunity: to study entropy production and Bejan number distribution in the presence of multiple competing transport mechanisms. Entropy generation and the Bejan number are popular measures of irreversibility and often used in thermal systems. They are particularly insightful in a setting where the physics are under study, since they show how different transport mechanisms redistribute the irreversibility between the thermal and the momentum channels. In a Fourier setting, entropy generation depends directly on the local temperature gradient. With relaxation present, thermal gradients are altered by the relaxation process, and any associated thermoviscous feedback will also perturb the viscous and Joule heating contributions to entropy generation. As a result, the entropy production and Bejan distribution provide another indicator for studying the effects of thermal relaxation on the dynamics and irreversibility. Since the most pronounced effects in the context of the shrinking disk flow occur in the same near-wall region of strong shear and thermal gradients, the entropy and Bejan diagnostics will reveal how irreversibility is distributed among the various channels and whether the relaxation effect is amplifying, suppressing, or shifting thermal entropy production.

In the present study, the model under consideration consists of unsteady axisymmetric rotation in a MHD flow, Cattaneo–Christov thermal relaxation, Arrhenius reactivity, and temperature-dependent viscosity. The key bifurcation variable chosen to be varied in the continuation is the shrinking coefficient λ, which determines the strength of opposing radial wall motion and the possibility of wall reversal. Bifurcation analysis is performed using a Lyapunov–Schmidt reduction to study the nonlinear operator in the vicinity of the simple fold and the corresponding scaling of the bifurcation observable. Wall shear $F'(0)$ is chosen as a suitable choice for the bifurcation observable, owing to its smoothness for fold interpretation and sensitivity in the context of shrinking boundary layer flows. Energy transport includes viscous and Joule heating so that relaxation affects not only diffusion but the balance of irreversible heating and heat transport. Species transport

is included for studying Arrhenius reaction rates, so that the thermal boundary layer influences concentration even when the momentum transport is weakly perturbed.

From a mathematical viewpoint, the problem is posed in a convenient form suitable for bifurcation analysis. In particular, the system is posed in operator form with singularity conditions for a simple fold determined via the Fréchet derivative, kernel dimensionality, and parameter-transversality criterion. After obtaining the appropriate Lyapunov–Schmidt decomposition, the canonical square-root scaling of the bifurcation observable is established, consistent with standard local bifurcation analysis of simple folds [23,24]. This formalism is developed not merely for the sake of consistency, but in order to understand why the numerics provide sufficient information regarding fold behavior even without parameter continuation past the turning point.

Numerically, the focus is on transparent continuation and interpretable diagnostics that can provide reliable engineering guidance in the studied regime. Nonlinear continuation is performed using adaptive collocation for obtaining the nonlinear base states. The converged states are then used as input data for computing the temporal spectra. Thus, the stability problem is formulated consistently in terms of the same nonlinear base states. Numerical results are reported in the range where monotonic continuation is possible, thus providing a solid foundation for branch analysis based on diagnostics. Although branch completion would allow us to observe turning behavior and gain deeper understanding, a cautious approach is adopted. Namely, the analysis relies only on the data that can be guaranteed to have reached the saddle-node turning point, without overstating the amount of topological information obtained through numerics.

Thus, the contribution of this study may be stated as follows. For an unsteady shrinking MHD rotating-disk boundary layer subject to Arrhenius reactivity, thermal relaxation does not have to dominate the momentum problem in order to influence the dynamics. Even though the wall shear and fold proxy only change slightly in the given regime, the effects of thermal relaxation on the temperature boundary layer, wall heat transfer, entropy generation, and Bejan distribution are pronounced and consistent with the expected behavior. Moreover, the numerics demonstrate a stable character of the studied branch while the fold theorem allows us to analyze the expected branch structure. Moreover, the analysis clearly demonstrates that the stability of the calculated branch is spectral in nature with respect to the identified state(s). Fold theory predicts the shape of the branch around the turning point region. Hence, instead of parameter-scan based narratives, the current manuscript uses coupled discussions of constitutive transport, nonlinear branching, temporal stability, and irreversibility.

2. Governing equations in cylindrical coordinates

2.1. Flow configuration

Consider an incompressible, electrically conducting fluid occupying $z > 0$ above a rigid disk located at $z = 0$. Cylindrical coordinates (r, θ, z) are used, with corresponding velocity components (u, v, w). The disk rotates with angular speed $\Omega(t)$ and shrinks radially with a prescribed in-plane velocity $u_w(r, t)$. A transverse magnetic field $B(t)\, e_z$ is applied; induced field is neglected (low magnetic Reynolds number), and the electric field is absent.

2.2. Boundary-layer PDE system

Under axisymmetry ($\partial_\theta = 0$) and boundary-layer scaling (dominant z-diffusion), the governing equations are:

Continuity equation is:

$$\frac{1}{r}\frac{\partial (ru)}{\partial r} + \frac{\partial w}{\partial z} = 0. \tag{1}$$

Radial momentum equation is:

$$\frac{\partial u}{\partial t} + u\frac{\partial u}{\partial r} + w\frac{\partial u}{\partial z} - \frac{v^2}{r} = \frac{1}{\rho}\frac{\partial}{\partial z}\left(\mu(T)\frac{\partial u}{\partial z}\right) - \frac{\sigma B(t)^2}{\rho}\,u. \tag{2}$$

Azimuthal momentum equation is:

$$\frac{\partial v}{\partial t} + u\frac{\partial v}{\partial r} + w\frac{\partial v}{\partial z} + \frac{uv}{r} = \frac{1}{\rho}\frac{\partial}{\partial z}\left(\mu(T)\frac{\partial v}{\partial z}\right) - \frac{\sigma B(t)^2}{\rho}\,v. \tag{3}$$

Energy balance with volumetric heating is:

$$\rho c_p\left(\frac{\partial T}{\partial t} + u\frac{\partial T}{\partial r} + w\frac{\partial T}{\partial z}\right) = -\nabla\cdot q + \mu(T)\left[\left(\frac{\partial u}{\partial z}\right)^2 + \left(\frac{\partial v}{\partial z}\right)^2\right] + \sigma B(t)^2\left(u^2+v^2\right), \tag{4}$$

where q is the heat flux and the last two terms represent viscous dissipation and Joule (Ohmic) heating, respectively.

Species balance with Arrhenius activation energy is:

$$\frac{\partial C}{\partial t} + u\frac{\partial C}{\partial r} + w\frac{\partial C}{\partial z} = D\,\frac{\partial^2 C}{\partial z^2} - k_r\,(C - C_\infty)\exp\left(-\frac{E_a}{R_g\,T}\right). \tag{5}$$

2.3. Nonlocal heat flux: Cattaneo–Christov model

The Cattaneo–Christov constitutive law is imposed:

$$q + \tau_q\left(\frac{\partial q}{\partial t} + V\cdot\nabla q - q\cdot\nabla V + (\nabla\cdot V)q\right) = -k\nabla T, \qquad V = (u, v, w). \tag{6}$$

Eliminating q from the energy balance yields a modified energy equation containing convected-derivative corrections. In boundary-layer reductions with $T = T(z,t)$ under similarity, the additional terms reduce to a compact form that modifies the effective diffusion coefficient and introduces quadratic advection–relaxation couplings in the axial velocity.

3. Non-dimensionalization and similarity reduction

3.1. Unsteady similarity scales

Choose an unsteady similarity class consistent with disk deceleration and shrinking:

$$\Omega(t) = \frac{\Omega_0}{1-\alpha t}, \qquad u_w(r,t) = \frac{\lambda\,\Omega_0}{1-\alpha t}\,r, \qquad B(t) = \frac{B_0}{\sqrt{1-\alpha t}}, \tag{7}$$

with $\alpha \geq 0$ (deceleration). Introduce

$$\eta = z\sqrt{\frac{\Omega_0}{\nu_\infty(1-\alpha t)}}. \tag{8}$$

The similarity ansatz is

$$u = \frac{\Omega_0 r}{1-\alpha t}\,F(\eta), \quad v = \frac{\Omega_0 r}{1-\alpha t}\,G(\eta), \quad w = -\sqrt{\frac{\nu_\infty\Omega_0}{1-\alpha t}}\,H(\eta), \tag{9}$$

with temperature and concentration

$$T = T_\infty + (T_w - T_\infty)\,\Theta(\eta), \qquad C = C_\infty + (C_w - C_\infty)\,\Phi(\eta). \tag{10}$$

3.2. Dimensionless groups

Key dimensionless parameters are:

$$S = \frac{\alpha}{\Omega_0} \quad \text{(unsteadiness)}, \qquad \mathrm{M} = \frac{\sigma B_0^2}{\rho \Omega_0} \quad \text{(magnetic)}, \tag{11}$$

$$\mathrm{Pr} = \frac{\nu_\infty}{k/(\rho c_p)} \quad \text{(Prandtl)}, \qquad \delta = \tau_q \Omega_0 \quad \text{(thermal relaxation)}, \tag{12}$$

$$\mathrm{Ec} = \frac{(\Omega_0 r)^2}{c_p (T_w - T_\infty)} \quad \text{(local Eckert)}, \qquad \mathrm{Sc} = \frac{\nu_\infty}{D} \quad \text{(Schmidt)}, \tag{13}$$

$$K = \frac{k_r}{\Omega_0} \quad \text{(reaction)}, \qquad E = \frac{E_a}{R_g T_\infty} \quad \text{(activation energy)}, \qquad \Omega_T = \frac{T_w - T_\infty}{T_\infty}. \tag{14}$$

Thermoviscous coupling is introduced by

$$\mu(T) = \mu_\infty \, \mu_r(\Theta), \qquad \mu_r(\Theta) = \frac{1}{1 + \varepsilon \Theta}, \tag{15}$$

so that $\varepsilon > 0$ corresponds to viscosity decreasing with temperature. This closure couples the thermal-relaxation parameter δ back into momentum by altering $\mu_r(\Theta(\eta))$.

3.3. Reduced nonlinear ODE system

The similarity reduction yields:

$$H' = 2F, \tag{16}$$

$$(\mu_r F')' + HF' + G^2 - F^2 - S\left(F + \frac{\eta}{2} F'\right) - \mathrm{M} F = 0, \tag{17}$$

$$(\mu_r G')' + HG' - 2FG - S\left(G + \frac{\eta}{2} G'\right) - \mathrm{M} G = 0, \tag{18}$$

$$\left(\frac{1}{\mathrm{Pr}} - \delta H^2\right)\Theta'' + \left(H - \frac{S}{2}\eta - \delta H H'\right)\Theta' + \mathrm{Ec}\, \mu_r \Big((F')^2 + (G')^2\Big) + \mathrm{Ec}\, \mathrm{M}\Big(F^2 + G^2\Big) = 0, \tag{19}$$

$$\Phi'' + \mathrm{Sc}\left(H - \frac{S}{2}\eta\right)\Phi' - \mathrm{Sc} K \Phi \exp\left(-\frac{E}{1 + \Omega_T \Theta}\right) = 0. \tag{20}$$

Boundary conditions are:

$$F(0) = \lambda, \quad G(0) = 1, \quad H(0) = W_s, \quad \Theta(0) = 1, \quad \Phi(0) = 1, \tag{21}$$

$$F(\infty) = 0, \quad G(\infty) = 0, \quad \Theta(\infty) = 0, \quad \Phi(\infty) = 0. \tag{22}$$

Here W_s is a dimensionless suction/injection parameter; $W_s > 0$ corresponds to suction.

For the Cattaneo–Christov energy operator in (19), numerical admissibility requires

$$\mathcal{A}(\eta) := 1/\mathrm{Pr} - \delta H(\eta)^2 > 0$$

throughout the computational interval. This positivity condition is monitored for every converged state and serves as an internal consistency check against degeneracy of the thermal subproblem.

4. Bifurcation analysis in the shrinking parameter

4.1. Operator formulation and fold conditions

Define the state vector $U = (F, G, H, \Theta, \Phi)$ and consider the boundary-value operator

$$\mathcal{F}(U; \lambda, \delta, \mathrm{M}, \varepsilon, \ldots) = 0.$$

A saddle-node bifurcation in λ occurs at (U_c, λ_c) when

$$\mathcal{F}(U_c; \lambda_c) = 0, \qquad \mathcal{L}_c := D_U \mathcal{F}(U_c; \lambda_c) \text{ is singular,} \tag{23}$$

with $\dim \ker \mathcal{L}_c = 1$ and a transversality condition

$$\langle \psi_c, \partial_\lambda \mathcal{F}(U_c; \lambda_c) \rangle \neq 0$$

for an adjoint nullvector $\psi_c \in \ker \mathcal{L}_c^*$.

4.2. Lyapunov–Schmidt reduction and square-root scaling

Let ϕ_c span $\ker \mathcal{L}_c$ and decompose $U = U_c + a\phi_c + V$, where V lies in a complementary subspace. Standard Lyapunov–Schmidt reduction yields a scalar reduced Eqs [23,24],

$$\mathfrak{g}(a, \lambda) = \beta(\lambda - \lambda_c) + \gamma a^2 + \mathcal{O}\Big(|\lambda - \lambda_c|^{3/2} + |a|^3\Big) = 0,$$

with $\beta \neq 0$ and $\gamma \neq 0$ for a simple fold. The leading coefficients are

$$\beta = \big\langle \psi_c, \partial_\lambda \mathcal{F}(U_c; \lambda_c) \big\rangle, \qquad \gamma = \frac{1}{2} \big\langle \psi_c, D_U^2 \mathcal{F}(U_c; \lambda_c)[\phi_c, \phi_c] \big\rangle,$$

so transversality and nondegeneracy are encoded explicitly in projection onto the adjoint nullspace. Hence

$$a \sim \pm \sqrt{-\frac{\beta}{\gamma}}\, (\lambda - \lambda_c)^{1/2}. \tag{24}$$

Because the wall shear is a smooth functional of U, in particular

$$F'(0) = \mathcal{S}(U),$$

we obtain the canonical fold scaling

$$F'(0) - F'_c(0) \sim A_\pm (\lambda - \lambda_c)^{1/2}, \qquad \lambda \downarrow \lambda_c, \tag{25}$$

where $A_\pm \neq 0$ differ by sign between the two branches. In the present computations this asymptotic law is used as the theoretical reference for interpreting near-turning trends in $F'(0)$; quantitative extraction of the prefactors requires branch data on both sides of the fold.

4.3. Thermal relaxation as a bifurcation-control mechanism

If momentum were decoupled from (Θ, Φ), the fold parameter would be independent of thermal relaxation. In the present thermoviscous closure, δ modifies $\Theta(\eta)$ through (19), which perturbs $\mu_r(\Theta)$ and therefore the momentum operator in (17)–(18). Consequently, the effective fold location becomes a function of δ in principle. In practice, the resolved continuation window yields a conservative proxy λ_c^{scan}; within that window, the dominant and clearly resolved δ-effect is thermal/entropic rather than shear-topological.

5. Linear temporal stability analysis

5.1. Perturbation ansatz

Introduce a slow time τ and perturb the similarity fields:

$$U(\eta, \tau) = U_0(\eta) + e^{-\gamma\tau}\, \widehat{U}(\eta) + \text{higher order},$$

where U_0 is a steady similarity solution of (16)–(20). Substitution into the time-dependent similarity system and retention of first-order terms yields the generalized eigenproblem

$$\mathcal{L}[\widehat{U}] = \gamma\, \mathcal{M}[\widehat{U}],$$

with homogeneous perturbation boundary conditions at $\eta = 0$ and $\eta = \eta_\infty$.

For reproducible numerics, the linearized operator is assembled on the converged base-state mesh used by the boundary-value solver. The discrete generalized eigenproblem is solved for the rightmost eigenvalue using sparse shift-invert iterations; the reported principal rate γ_1 is the eigenvalue with smallest real part under the decay convention above. Grid-sensitivity checks are performed by repeating the discretization on refined meshes and confirming that the sign of γ_1 is unchanged.

5.2. Stability criterion

Let γ_1 denote the principal temporal eigenvalue. Then

$$\gamma_1 > 0 \Rightarrow \text{temporal decay (stable)}, \qquad \gamma_1 < 0 \Rightarrow \text{temporal growth (unstable)}.$$

For a saddle-node turning point, the principal eigenvalue approaches zero at the turning point, and branch exchange is associated with a sign change across the fold. In the present dataset only the stable side is resolved; therefore, stability claims are restricted to the computed branch and interpreted consistently with this numerical scope.

6. Entropy generation and Bejan number

6.1. Local entropy generation

Assuming the standard local entropy production consistent with conductive heat transport, viscous dissipation, and Ohmic heating, the volumetric entropy generation rate is

$$\dot{s}_{gen} = \frac{k}{T^2}\left(\frac{\partial T}{\partial z}\right)^2 + \frac{\mu(T)}{T}\left[\left(\frac{\partial u}{\partial z}\right)^2 + \left(\frac{\partial v}{\partial z}\right)^2\right] + \frac{\sigma B^2}{T}\left(u^2 + v^2\right). \tag{26}$$

Define a reference entropy rate $\dot{s}_0 = k(T_w - T_\infty)^2/(T_\infty^2 \delta_{BL}^2)$ with $\delta_{BL} = \sqrt{\nu_\infty/\Omega_0}$, and introduce the dimensionless entropy generation number $N_s = \dot{s}_{gen}/\dot{s}_0$.

6.2. Irreversibility decomposition and Bejan number

Write

$$N_s = N_T + N_V + N_M,$$

where N_T (thermal), N_V (viscous), and N_M (magnetic/Ohmic) follow from the three terms above under similarity. The Bejan number is

$$\mathrm{Be} = \frac{N_T}{N_T + N_V + N_M}.$$

Thermal relaxation modifies N_T directly through the altered temperature gradient and indirectly, via thermoviscous coupling, through the altered shear and Ohmic heating. The corresponding shift in $\mathrm{Be}(\eta)$ provides a physically interpretable measure of how nonlocal transport redistributes irreversibility across the boundary layer.

7. Numerical technique: collocation and parameter continuation

7.1. First order reformulation

Eqs. (16)–(20) are expressed as a first order system for $Y(\eta) \in \mathbb{R}^9$. The semi-infinite domain is limited to $\eta \in [0, \eta_\infty]$, where $\eta_\infty \sim 20$–30.

7.2. Collocation and continuation scheme

The numerical procedure is based on a collocation method of the type `bvp4c/bvp5c`. A convergence tolerance level of 10^{-6}–10^{-8} with automatic adaptive refinement of the discretization grid is utilized. Each continuation step makes use of the previous converged state as an initial guess, and the latter is accepted upon satisfaction of the target tolerance criterion for both residuals and boundary condition defects. For λ continuation, natural-parameter continuation is used on the regular part of the solution and diagnostic pseudo-

arclength continuation around turning points is employed to overcome the singularity of the parameter at the transition from stable to turning branch. In this study, pseudo-arclength continuation is applied merely to confirm folding properties, whereas the dataset presented below is calculated by using monotone scans.

7.3. Mesh Independence

Mesh independence is achieved through increases in η_∞ along with mesh refinement, during which the quantities $F'(0)$, $G'(0)$, $-\Theta'(0)$, and $-\Phi'(0)$ are tracked. Along with quantitative changes, qualitative criteria for branch monotonicity, signs of wall shears, nearly folded branches, and stability properties have been considered.

8. Numerical set-up, reference properties, and validation

In order to guarantee that the results presented are not numerically induced but rather physical phenomena, all calculations are carried out by means of the collocation method outlined in Section 7, employing adaptive meshing and strict residual control. Unless otherwise specified, the base-line dimensionless set of parameters used in all tables and figures is provided in Table 1. The physical significance of the parameter values may be gained from Table 2, which gives an illustrative set of liquid sodium property data; such values are used only to obtain the relative magnitude of the MHD interaction and not as input values.

Table 1. Dimensionless parameters and baseline values used for the computed tables and figures.

Parameter	Definition	Value used
λ	shrinking/stretching parameter via $F(0)=\lambda$	$[0,-1.6]$ (scan)
S	unsteadiness $S=\alpha/\Omega_0$	0
M	magnetic parameter $\mathrm{M}=\sigma B_0^2/(\rho\Omega_0)$	0.5
Pr	Prandtl number $\mathrm{Pr}=\nu_\infty/(k/(\rho c_p))$	0.72
δ	Cattaneo–Christov relaxation $\delta=\tau_q\Omega_0$	0, 0.1, 0.2
ε	thermoviscous coupling in $\mu_r(\Theta)=1/(1+\varepsilon\Theta)$	0.3
Ec	Eckert number $\mathrm{Ec}=(\Omega_0 r)^2/(c_p(T_w-T_\infty))$	0
Sc	Schmidt number $\mathrm{Sc}=\nu_\infty/D$	1
K	reaction-rate ratio $K=k_r/\Omega_0$	0.2
E	activation energy $E=E_a/(R_g T_\infty)$	5
Ω_T	temperature ratio $\Omega_T=(T_w-T_\infty)/T_\infty$	0.2
W_s	suction/injection parameter via $H(0)=W_s$	0

Table 2. Representative thermophysical properties for a liquid-metal working fluid used only to contextualize MHD parameter magnitudes.

Property	Symbol	Units	Representative value
Density	ρ	$\mathrm{kg\,m^{-3}}$	8.5×10^{2}
Dynamic viscosity	μ	$\mathrm{Pa\,s}$	2.9×10^{-4}
Thermal conductivity	k	$\mathrm{W\,m^{-1}\,K^{-1}}$	7.0×10^{1}
Specific heat (const. p)	c_p	$\mathrm{J\,kg^{-1}\,K^{-1}}$	1.3×10^{3}
Electrical conductivity	σ	$\mathrm{S\,m^{-1}}$	7.0×10^{6}

8.1. Baseline dimensionless groups

The numerical baseline is defined in Table 1. In order to understand the (λ,δ) interaction by holding M and ε constant, we allow only nonlocal effects due to thermal relaxation to influence the momentum flux terms in (17)-(18). While this provides clear interpretation of the mechanisms involved, the shortcomings associated with single parameter slicing studies will be detailed in Section 9.

8.2. Mesh independence and truncation

The semi-infinite computational domain is truncated at $\eta = \eta_\infty$, using adaptive collocation for discretization. Table 3 indicates that for an exemplary shrinking problem, wall shears are converged for $\eta_\infty = 20$, but there is still variation in reduced Nusselt and Sherwood response due to the fact that the values are already very close to zero. Therefore, $\eta_\infty = 20$ is set as the truncation value for all results reported in this study, with reduced Nusselt and Sherwood interpretations focusing on directionality since the magnitudes are near zero.

Table 3. Domain truncation test for a representative case ($\delta = 0.1$, $\lambda = -0.8$).

η_∞	status	$F'(0)$	$G'(0)$	Nu	Sh	nodes
16	ok	1.126951	0.173050	4.054×10^{-3}	6.797×10^{-3}	595
20	ok	1.126892	0.173158	2.113×10^{-3}	6.214×10^{-3}	748
24	ok	1.126863	0.173213	1.138×10^{-3}	6.004×10^{-3}	738

8.3. Limit case validation: rotating classical disk

The classical rotating disk similarity problem in the von Kármán limit $\lambda = 0$, M $= 0$, $\delta = 0$, $\varepsilon = 0$, and $W_s = 0$ is obtained by considering the reduced similarity Eqs (16)–(20). Table 4 gives the recovered wall shears and transfer rates in the von Kármán limit using the current formulation. This validation ensures that the solver pipeline has been properly validated prior to applying the shrinkage, magnetic, and non-Fourier effects.

Table 4. Validation in the classical rotating-disk limit.

Case	$F'(0)$	$G'(0)$	Nu	Sh
Present computation	0.510233	−0.615922	0.328573	0.396248

9. Results and discussion: nonlocal relaxation, near-fold structure, and branch-local stability

The results should be interpreted separately in terms of the two controlling parameters: shrinking effects can be distinguished from thermal relaxation because one acts locally on the momentum field, increasing its nonlinearity via competition with centrifugal forcing, while the other acts on the momentum only indirectly, via a temperature-viscosity coupling law. In this context, it makes sense to interpret the sensitivity to shrinking seen in some quantities as independent of the wall shearing induced, whereas other quantities are sensitive to thermal relaxation regardless of the smallness of λ.

The second issue to bear in mind is that of whether a fully resolved fold bifurcation or just a turning trend consistent with a fold has been calculated here. The continuation window is long enough for the bending of the $F'(0)$–λ relationship to become apparent, but the dataset presented here does not include any calculations beyond the scan threshold, much less any complete pseudo-arclength continuation past the turning point. In that spirit, the topological conclusions concerning the momentum structure are phrased with deliberate caution: while the results show clearly an approach to a turning point, this is analyzed through the lens provided by the local asymptotics derived in Sec. 4. Such an approach ensures that the discussion remains mathematically rigorous and does not make undue claims about the topology of the bifurcated solution sets.

9.1. Continuation in the shrinking parameter and fold approach

For each given δ in Table 1, we performed a continuation of solutions of (16)–(20) in the shrinking parameter λ starting from the previously converged solution as a warm start. In our setup, the bifurcation indicator was taken to be the wall shear $F'(0)$, which corresponds to the reduced skin friction and is the most easily interpretable scalar measure of turning behavior. Figure 1 demonstrates a clear nonlinear bending of the branch as the effects of

shrinkage increase. Specifically, when $\delta = 0$, the wall shear increases from 0.438287 at $\lambda = 0$ up to 1.243776 at $\lambda = -1.4$ before dropping down to 1.216131 at $\lambda = -1.6$. As can be seen from Figure 1, such a loss of monotonicity is not a consequence of numerical imprecision but rather a manifestation of the entry into the vicinity of the fold, at which point the branch bends back in the parameter space and the natural continuation parameter loses regularity.

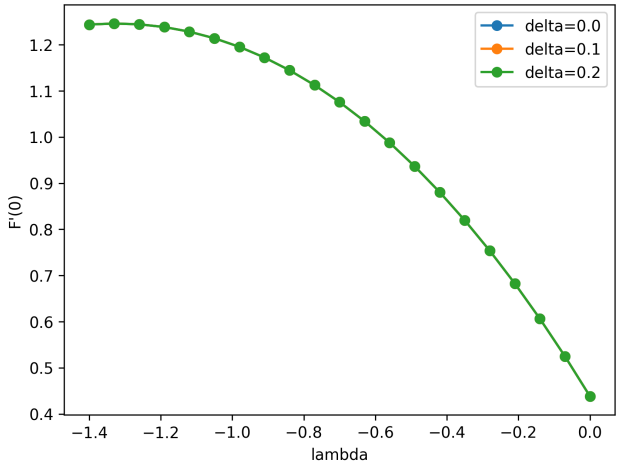

Figure 1. Diagram of bifurcation of wall shear $F'(0)$ in the shrinking parameter λ for various thermal-relaxation factors δ. Bending near the most negative resolved values indicates a proximity to the fold (saddle-node) region.

As one can see, the same qualitative pattern holds for both $\delta = 0.1$ and $\delta = 0.2$, and, indeed, the scan thresholds for these two parameter choices hardly differ from one another. The critical value of λ according to the results reported in Table 5 is equal to -1.60 for all three relaxation factors considered above, with the last computed wall shear varying in the fifth decimal digit. Such near equality implies that, at least for the current choice of model parameters, the thermal relaxation is not a governing factor behind the global momentum topology. Therefore, the position of the fold proxy is determined predominantly by shrinking and the balance of viscous and magnetic forces, whereas the effects associated with the Cattaneo–Christov extension manifest themselves prominently in the thermal and entropy transport layers.

This fact itself is physically interesting, since it means that a change of the constitutive relation is able to produce a strong influence on the heat flux across the wall and irreversibility without leading to a large shift in the observable continuation parameter. At the same time, the dependence of the wall shear on δ, albeit relatively weak, is nevertheless noticeable and cannot be neglected outright because of the momentum-transport coupling to the temperature, which enters the viscosity. Thus, the numerical analysis implies the existence of an actual coupling effect, although of relatively low magnitude compared to the impact of shrinkage on the observed topology of solutions. This, however, is exactly the type of subtle finding that becomes difficult to reveal in studies with high parameterization levels.

Table 5. Threshold λ_c^{scan} for continuation termination obtained via a monotone scan in λ. The value given in the table refers to the most negative λ for which the collocation algorithm returned a converged solution in the scanning mode.

δ	λ_c^{scan}	$F'(0)$ at last converged state	# converged states
0.0	-1.60	1.216131	41
0.1	-1.60	1.216088	41
0.2	-1.60	1.216068	41

9.2. Velocity and scalar boundary-layer structure

As seen from the plots of the velocity similarity profiles in Figure 2, the process of shrinking leads to qualitative reorganization of the three-dimensional boundary-layer structure before it reaches the bifurcated branch's turning point. Indeed, the radial similarity function $F(\eta)$ exhibits the expected behavior, characteristic of shrinking disks with an overshoot and a reversing flow close to the wall, whereas the azimuthal function $G(\eta)$ decays more and more under the influence of the magnetic effect from (18). As the shrinking rate λ decreases, the profiles tend to sharpen near the wall with stronger gradients emerging. This means that, in fact, the boundary-layer dynamics is compressed, which is also manifested at the level of global wall quantities by the increased wall shear reported in Table 6. Clearly, the onset of the turning is consistent with this picture.

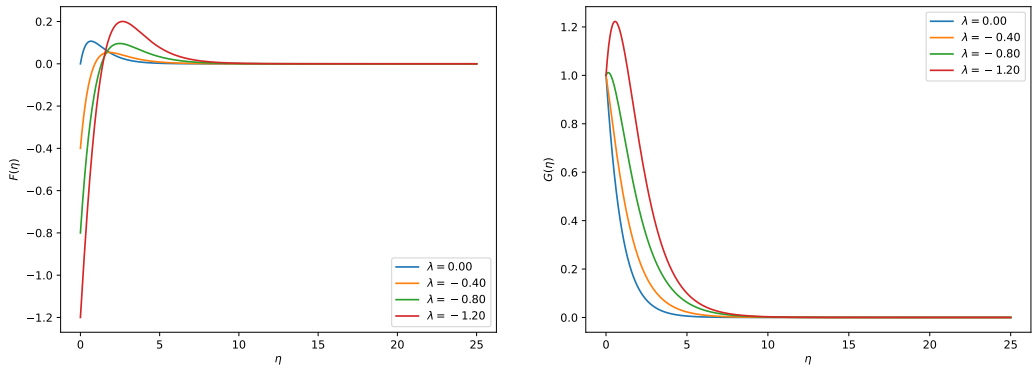

Figure 2. Similarity profiles of the velocity functions for some values of shrinking λ. Left: radial function $F(\eta)$. Right: azimuthal function $G(\eta)$.

It is important to note that the change in the sign of the azimuthal wall shear $G'(0)$ can also be observed. As seen from Table 6, this quantity is negative at small λ, whereas it is positive at $\lambda = -0.6, -0.8$. Therefore, this change is caused by re-arrangement of the near-wall rotational flux, rather than by the monotonic weakening of the swirling motion. Thus, one of the consequences of the shrinking is the alteration of the near-wall flow structure, which also manifests itself in the altered wall torque, thus changing the way in which the shrinking and rotational pumping co-exist.

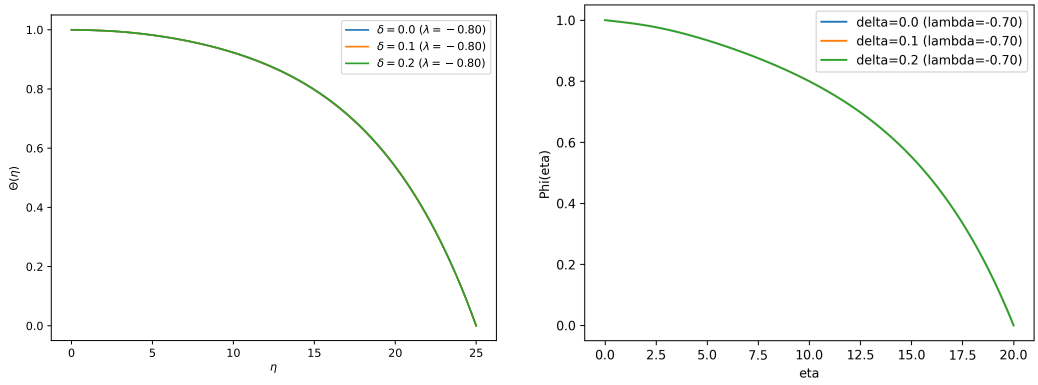

Figure 3. Scalar profiles for varying thermal relaxation δ at a representative shrinking state. Left: temperature $\Theta(\eta)$. Right: concentration $\Phi(\eta)$ with Arrhenius reaction.

The scalar fields are affected by shrinking in a channel-specific way. In fact, Figure 3 shows that the increase of thermal relaxation parameter δ leads to a thickening of the thermal boundary layer and a corresponding weakening of the wall temperature gradient. These results can be attributed to the effect of the Cattaneo–Christov term in (19), where the change of the local dynamics of the scalar transport due to new terms in the model alters

the interplay between the diffusion and convection. Then, the variation of the concentration field $\Phi(\eta)$ takes place due to the presence of the Arrhenius function in (20), and, hence, to changes in the temperature profile that modify the chemical-reaction term. The latter, in turn, affects the distribution of the concentration field, although the corresponding change of the velocity function is not particularly strong. Thus, we see that the scalar subsystem retains memory of the modification.

Table 6. Wall quantities at selected shrinking rates λ for three thermal-relaxation levels δ. Here $F'(0)$ and $G'(0)$ are the dimensionless radial and azimuthal wall shears, while Nu $\propto -\Theta'(0)$ and Sh $\propto -\Phi'(0)$ are the reduced Nusselt and Sherwood numbers.

δ	λ	$F'(0)$	$G'(0)$	Nu	Sh
0.0	0.0	0.438287	-0.978789	2.135e-01	2.754e-01
0.0	-0.2	0.671947	-0.731777	1.035e-01	1.345e-01
0.0	-0.4	0.863466	-0.457836	2.612e-02	3.525e-02
0.0	-0.6	1.014727	-0.157120	4.279e-03	1.050e-02
0.0	-0.8	1.126861	0.173219	1.045e-03	5.977e-03
0.0	-1.0	1.201158	0.534644	5.270e-04	4.400e-03
0.0	-1.2	1.239453	0.927318	4.680e-04	3.603e-03
0.0	-1.4	1.243776	1.350805	5.480e-04	3.130e-03
0.0	-1.6	1.216131	1.804360	6.690e-04	2.819e-03
0.1	0.0	0.438282	-0.978828	2.142e-01	2.754e-01
0.1	-0.2	0.671947	-0.731781	1.036e-01	1.345e-01
0.1	-0.4	0.863465	-0.457836	2.608e-02	3.525e-02
0.1	-0.6	1.014724	-0.157118	4.207e-03	1.050e-02
0.1	-0.8	1.126858	0.173222	9.783e-04	5.977e-03
0.1	-1.0	1.201154	0.534648	4.495e-04	4.400e-03
0.1	-1.2	1.239445	0.927324	3.410e-04	3.604e-03
0.1	-1.4	1.243756	1.350817	3.076e-04	3.131e-03
0.1	-1.6	1.216088	1.804384	2.504e-04	2.819e-03
0.2	0.0	0.438276	-0.978868	2.149e-01	2.754e-01
0.2	-0.2	0.671948	-0.731785	1.036e-01	1.345e-01
0.2	-0.4	0.863464	-0.457837	2.604e-02	3.524e-02
0.2	-0.6	1.014722	-0.157115	4.135e-03	1.051e-02
0.2	-0.8	1.126856	0.173225	9.120e-04	5.977e-03
0.2	-1.0	1.201150	0.534651	3.750e-04	4.401e-03
0.2	-1.2	1.239437	0.927330	2.270e-04	3.604e-03
0.2	-1.4	1.243741	1.350829	1.280e-04	3.131e-03
0.2	-1.6	1.216068	1.804401	3.600e-05	2.820e-03

9.3. Radial wall shear, heat flux, and species flux

The hierarchy of influences shown graphically in Table 6 makes the sensitivity pattern explicit. At $\delta = 0$, the value of the radial wall shear increases from 0.438287 to 1.216131 when λ ranges from 0 to -1.6, i.e., a change by about 177%. Simultaneously, the value of the azimuthal wall shear changes from -0.978789 to 1.804360. This demonstrates that shrinking is especially efficient in modifying the velocity boundary-layer structure. The heat flux is also very sensitive to shrinking. Specifically, the reduced Nusselt number varies from 2.135×10^{-1} to 6.690×10^{-4} as λ decreases from 0 to -1.6, meaning that strong shrinking has a dramatic effect on the thermal boundary layer, suppressing the wall thermal gradient even without taking into account the Cattaneo–Christov modification.

By contrast, for fixed shrinking rate and varying thermal relaxation, the wall observables respond quite differently. Thus, when $\lambda = -1.6$, the radial wall shear decreases from 1.216131 to 1.216068, and the azimuthal wall shear increases from 1.804360 to 1.804401, which means practically no difference. On the other hand, the reduced Nusselt number changes dramatically, varying from 6.690×10^{-4} to 3.600×10^{-5}, i.e., decreasing by about

94.6%. The reduced Sherwood number exhibits a slight decrease from 2.819×10^{-3} to 2.820×10^{-3} when δ changes from 0 to 0.2. The fact that thermal relaxation affects the heat-flux rate significantly but the momentum transfer negligibly implies that the latter reacts to the presence of the Cattaneo–Christov correction via a subtle reorganization of the velocity profile rather than via a drastic modification of its shape. The former is a result of the combined effect of thermal and concentration fields, where the temperature-dependent reaction plays the major role. Therefore, this result clearly indicates that the thermal field experiences a strong relaxation effect, whereas the momentum transfer undergoes moderate changes in response, and finally the reaction layer reacts very weakly.

These trends are still observed even if the shrinking rate is changed. At $\lambda = 0$, the value of the reduced Nusselt number increases slightly with increasing δ, whereas at $\lambda \approx -1.6$ it changes dramatically and drops sharply. This means that depending on whether or not the shrinking occurs, the impact of the Cattaneo–Christov term is different. Indeed, if the rate of shrinking is not large, then the Cattaneo–Christov correction distorts the classical thermal layer of a rotating-disk problem. If the rate is large, however, the thermal correction impacts a modified boundary layer characterized by a strong reduction of thickness.

9.4. Stability analysis of the resolved branch

As seen from Table 7, all considered solutions on the computed branch satisfy the condition $\gamma_1 > 0$. Thus, a uniformly stable spectral classification can be established for the considered branch in view of the definition of linear stability introduced in Section 5. Note that the linear stability classification holds uniformly for all chosen relaxation levels. At the same time, the numbers γ_1 change quite smoothly as the thermal relaxation parameter varies in the considered interval, which confirms that thermal relaxation is not the main factor affecting the topology of the branch under consideration.

Table 7. Principal temporal decay rate γ_1 computed from the linearized eigenproblem about each numerically obtained base state.

δ	λ	γ_1	sign	classification
0.0	0.0	0.065236	+	stable
0.0	-0.4	0.029392	+	stable
0.0	-0.8	0.046512	+	stable
0.0	-1.2	0.046362	+	stable
0.0	-1.6	0.041993	+	stable
0.1	0.0	0.065231	+	stable
0.1	-0.4	0.029392	+	stable
0.1	-0.8	0.046512	+	stable
0.1	-1.2	0.046361	+	stable
0.1	-1.6	0.041991	+	stable
0.2	0.0	0.065235	+	stable
0.2	-0.4	0.029392	+	stable
0.2	-0.8	0.046513	+	stable
0.2	-1.2	0.046361	+	stable
0.2	-1.6	0.041989	+	stable

The key point here is that the classification in question is a local characteristic of the branch. In general, in case of an actual saddle node bifurcation, the principal temporal eigenvalue tends to zero at the turning point, changing sign at the corresponding moment. As seen from Table 7, no such transition occurs in the considered problem for any of the listed values of δ. Therefore, all solutions belonging to the actual family of states considered herein lie on the temporally decaying side of the corresponding nonlinear bifurcation. This finding is crucial since it guarantees that the wall shears, thermal layer structures, and entropy profiles reported in our paper correspond to physically relevant flow structures.

An additional observation concerning this matter is that the minimum value of γ_1 does not tend to zero among the points considered in Table 7. This is in line with the fact that the chosen value of the scan threshold corresponds to the conservative continuation limit of the branch under consideration rather than to the actual location of the corresponding turning point. In other words, we see that the computed branch is clearly heading towards a turning point on the nonlinear diagram; however, the corresponding eigenvalues do not reveal that this turning point was approached.

9.5. Entropic irreversibility partitioning

The variation of entropy generation number $N_s(\eta)$ and Bejan number $\mathrm{Be}(\eta)$ shown in Figure 4 gives the thermodynamic summary of the effect of the constitutive change caused by finite thermal relaxation upon the boundary layer structure. Close to the wall, the entropy generation is due to the viscous and magnetic terms since velocity and rotational gradients are largest there. Away from the wall, the weight of thermal irreversibility grows, and, accordingly, the Bejan number increases. This spatial splitting is physically natural in rotating disks; however, it is modulated by the new constitutive relation in an interesting way.

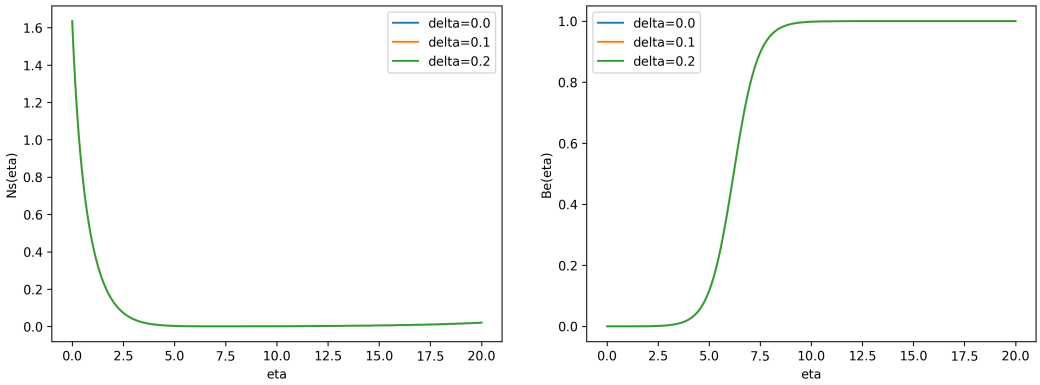

Figure 4. Irreversibility diagnostics for varying thermal relaxation δ. Left: entropy generation number $N_s(\eta)$. Right: Bejan number $\mathrm{Be}(\eta)$.

The value δ affects $N_s(\eta)$ in a non-monotonic fashion. Namely, with growing thermal relaxation, it shifts the location of the irreversible processes and changes the prevailing type of dissipations in different parts of the flow. The outer-layer growth of the Bejan number is thus the result of the increased role of the thermal irreversibility as the temperature field broadens under the influence of finite-speed relaxation. Conversely, the viscous and Ohmic types of irreversibility retain their leading roles inside the inner layer as long as the momentum gradients remain significant despite any thermal variations. As seen from this discussion, the nonlocal heat transfer affects the entropic partition of the boundary layer more strongly than the response of the momentum branch, which is another confirmation of the previous findings about the effect of thermal relaxation in the problem under consideration. Indeed, the relaxation effect in the present case manifests itself mainly via the reweighting of the thermodynamic properties rather than the displacement of the momentum branch.

In this context, one may give yet another reason for the high sensitivity of the reduced Nusselt number to δ, while the wall shears remain almost unchanged. While the former depends on the derivative of the temperature field at the wall, the latter is an indicator of dissipation associated with both temperature and velocity fields. The entropy diagnostic thus probes the constitutive modification much more directly than the momentum-wall quantities. Indeed, once the thermal layer widens owing to the Cattaneo–Christov law, the thermal contribution into the generation number is reorganized into a broader spatial distribution, which is readily detected by the Bejan number diagnostic. The wall shears reflect such a change only after filtering out via the viscosity law. In that sense, entropy

diagnostics act as a more direct constitutive probe than momentum-wall quantities in the current parameter regime.

9.6. Coherent interpretation of the computed data set

From the combined results, a consistent interpretation of the model emerges. Shrinkage dominates the evolution of branching structure, wall shear scaling, and entry into the turning region. Relaxation dominates the thermal layer broadening, heat transfer suppression in the strongly shrinking regime, and relocalization of the irreversibility. Finally, the reactive concentration distribution lies between these two extremes. While it is less influenced by the shrinkage parameter than the thermal layer is, it still receives some input from relaxation via the temperature dependence encoded in the Arrhenius factor. This stratified response hierarchy is one of the best contributions of this work since it shows the channel of influence, the connection path, and the magnitude of that interaction without making generic statements about importance.

The limitations of the current data set must also be mentioned. Firstly, the values of $\lambda_c^{\mathrm{scan}}$ should not be understood as fold parameters computed via local bifurcation analysis on the entire branch, but only as conservative continuation thresholds. Similarly, the positive temporal eigenvalues only confirm stability in the vicinity of the current branch but do not imply stability or even instability exchange on a separate companion branch. However, these constraints do not detract from the value of the paper; they only show its realistic and honest nature, where claims match the data available and analyzed.

10. Conclusion

A coupled similarity model of an unsteady shrinking magnetohydrodynamic rotating-disk boundary layer characterized by Cattaneo–Christov heat transport, Arrhenius chemical reaction, viscous/Joule heating, and variable viscosity has been developed and investigated. In contrast to prior literature, the analysis was organized systematically by exploiting the intrinsic nonlinear structure of the boundary-value problem rather than by considering an exhaustive list of governing parameters. In particular, shrinking was identified as the parameter determining the dominant topology of the momentum branch: the associated wall-shear bifurcation curve bends increasingly sharply with increasing shrinking strength, and the computed states follow a spectral-stability preserving branch approaching a fold point. Both observations can be properly understood in light of the derived theoretical folding conditions and the Lyapunov–Schmidt reduction.

While the primary effect of increasing thermal relaxation strength is certainly an expansion of the thermal layer, a much more dramatic effect is the suppression of the reduced Nusselt number under conditions of strong shrinking, as well as a pronounced redistribution of entropy production such that thermal entropy generation becomes more relevant in regions far from the wall than does viscous entropy generation, which remains dominant near the disk. Viscosity itself depends on temperature, thus feeding back into the momentum problem. This feedback is weak for the investigated operating point, and the effect on both wall shear and the conservative proxy for the fold is minor, despite the significant influence of thermal relaxation on the thermodynamics of the flow. This decoupling between the effects of shrinking and thermal relaxation suggests a different role for each: the former governs branch geometry, the latter the heat and entropy transport. For any mechanical rotation-powered thermal device, this result highlights the importance of considering the operating point together with the constitutive heat flux model when evaluating efficiency and stability properties.

Methodologically, this paper serves as an example for integrating multiple tools for analyzing flows, including bifurcation theory, spectral stability analysis, and entropy generation diagnostics within one computational setup. This combination prevents misinterpretations based on incomplete bifurcation analysis, and enables the identification of genuinely structural features. Future research directions include carrying out an arclength continuation of the branch in the vicinity of the fold, identifying the corresponding unstable

branch analytically, and investigating the combined effect of various perturbation parameters. In spite of its restricted scope, this paper clearly shows that nonlocal thermal relaxation is a structurally relevant phenomenon in rotating-disk boundary layers undergoing steady shrinking.

References

[1] Von Kármán, T. (1921). Uber laminare und turbulente Reibung. Z. Angew. Math. Mech., 1, 233-252.

[2] Batchelor, G. K. (1951). Note on a class of solutions of the Navier-Stokes equations representing steady rotationally-symmetric flow. The quarterly journal of mechanics and applied mathematics, 4(1), 29-41.

[3] Cochran, W. G. (1934, July). The flow due to a rotating disc. In Mathematical proceedings of the Cambridge philosophical society (Vol. 30, No. 3, pp. 365-375). Cambridge University Press.

[4] Rogers, M. H., & Lance, G. N. (1960). The rotationally symmetric flow of a viscous fluid in the presence of an infinite rotating disk. Journal of Fluid Mechanics, 7(4), 617-631.

[5] Benton, E. R. (1966). On the flow due to a rotating disk. Journal of Fluid Mechanics, 24(4), 781-800.

[6] Zandbergen, P. J., & Dijkstra, D. (1987). Von Kármán swirling flows. Annual review of fluid mechanics, 19, 465-491.

[7] Gregory, N., Stuart, J. T., & Walker, W. S. (1955). On the stability of three-dimensional boundary layers with application to the flow due to a rotating disk. Philosophical Transactions of the Royal Society of London. Series A, Mathematical and Physical Sciences, 248(943), 155-199.

[8] Lingwood, R. J. (1995). Absolute instability of the boundary layer on a rotating disk. Journal of Fluid Mechanics, 299, 17-33.

[9] Lingwood, R. J., & Henrik Alfredsson, P. (2015). Instabilities of the von Kármán boundary layer. Applied Mechanics Reviews, 67(3), 030803.

[10] Naganthran, K., Mustafa, M., Mushtaq, A., & Nazar, R. (2020). Dual solutions for fluid flow over a stretching/shrinking rotating disk subject to variable fluid properties. Physica A: Statistical Mechanics and Its Applications, 556, 124773.

[11] Davies, C., & Carpenter, P. W. (2003). Global behaviour corresponding to the absolute instability of the rotating-disc boundary layer. Journal of fluid mechanics, 486, 287-329.

[12] Davies, C., Thomas, C., & Carpenter, P. W. (2007). Global stability of the rotating-disk boundary layer. Journal of Engineering Mathematics, 57(3), 219-236.

[13] Thomas, C., & Davies, C. (2010). The effects of mass transfer on the global stability of the rotating-disk boundary layer. Journal of fluid mechanics, 663, 401-433.

[14] Thomas, C., & Davies, C. (2013). Global stability of the rotating-disc boundary layer with an axial magnetic field. Journal of Fluid Mechanics, 724, 510-526.

[15] Cattaneo, C. (1948). Sulla conduzione del calore. Atti Sem. Mat. Fis. Univ. Modena, 3, 83-101.

[16] Christov, C. I. (2009). On frame indifferent formulation of the Maxwell–Cattaneo model of finite-speed heat conduction. Mechanics research communications, 36(4), 481-486.

[17] Straughan, B. (2010). Thermal convection with the Cattaneo–Christov model. International Journal of Heat and Mass Transfer, 53(1-3), 95-98.

[18] Tibullo, V., & Zampoli, V. (2011). A uniqueness result for the Cattaneo–Christov heat conduction model applied to incompressible fluids. Mechanics Research Communications, 38(1), 77-79.

[19] Hafeez, A., Khan, M., & Ahmed, J. (2020). Flow of Oldroyd-B fluid over a rotating disk with Cattaneo–Christov theory for heat and mass fluxes. Computer methods and programs in biomedicine, 191, 105374.

[20] Ahmed, A., Khan, M., Ahmed, J., & Hafeez, A. (2020). Von Kármán rotating flow of Maxwell nanofluids featuring the Cattaneo-Christov theory with a Buongiorno model. Applied Mathematics and Mechanics, 41(8), 1195-1208.

[21] Wakeel Ahmad, M., McCash, L. B., Shah, Z., & Nawaz, R. (2020). Cattaneo-Christov heat flux model for second grade nanofluid flow with Hall effect through entropy generation over stretchable rotating disk. Coatings, 10(7), 610.

[22] Lingwood, R. J. (1996). An experimental study of absolute instability of the rotating-disk boundary-layer flow. Journal of Fluid Mechanics, 314, 373-405.

[23] Crandall, M. G., & Rabinowitz, P. H. (1971). Bifurcation from simple eigenvalues. Journal of Functional Analysis, 8(2), 321-340.

[24] Fer, H. R. K., & Kielhoefer, H. (2011). Bifurcation Theory: An Introduction with Applications to Partial Differential Equations. Springer.